An Introduction of "Utilization of Meteorological Satellite Data in Cloud Analysis"

Shiro Omori
Senior Coordinator for Satellite Data Quality,
Meteorological Satellite Center (MSC),
Japan Meteorological Agency (JMA)

Overview of the book

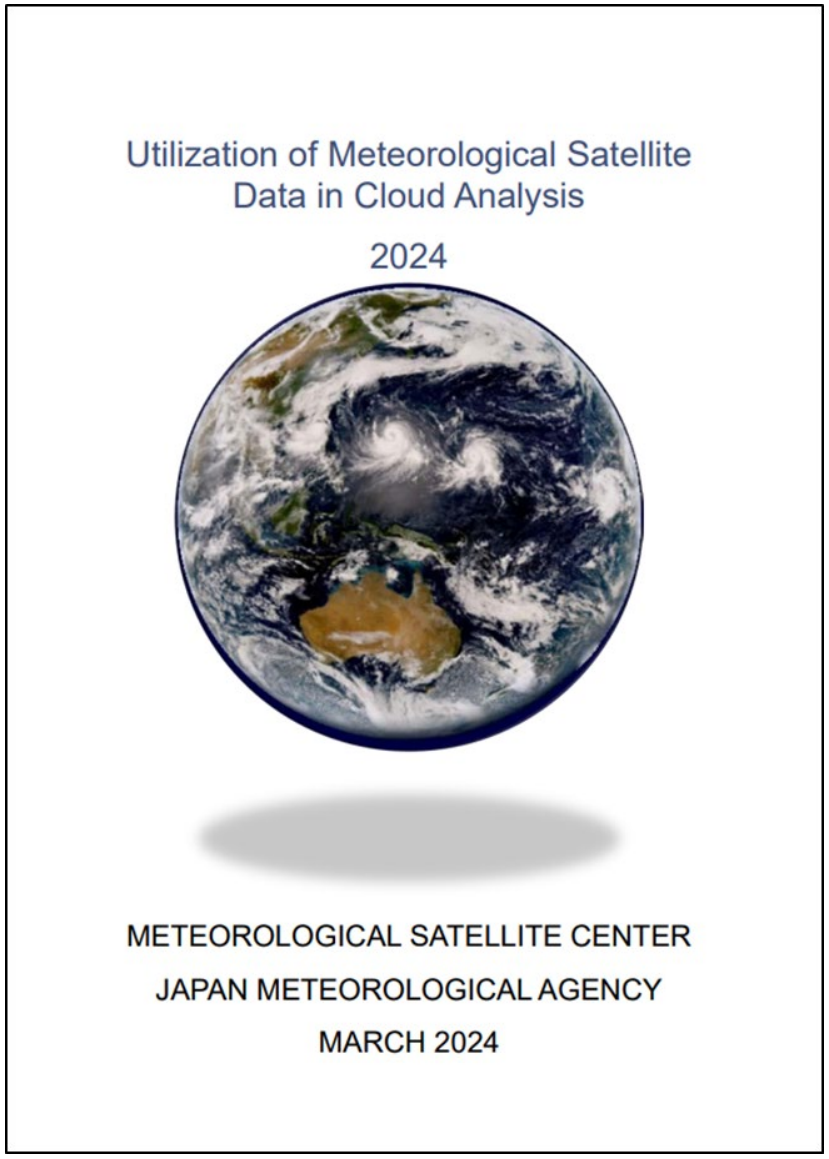

- Online distribution only

  https://www.data.jma.go.jp/mscweb/technotes/UtilizationMetSatData.pdf

  (Please download PDF file via the Internet)

- To explain how to utilize satellite imagery to meteorological analysis
  - This book contains many actual imagery, weather chart and some cloud photograph

- This book has as much as 283 pages.
  - But you can read a selected topic that you interests.

In my presentation, I'll show some pages of the book and introduce briefly.

Table of Contents of the book

Chapter 1

Outline of Meteorological Satellite Observation

1.1 Observation by Meteorological Satellites

1. Outline of Meteorological Satellite Observation

1.1. Observation by Meteorological Satellites

An advantage of meteorological satellite-based observation is the capacity for consistent worldwide monitoring with high spatial resolution. It enables monitoring of short-term atmospheric phenomena such as the development of cumulonimbus masses, cloud areas in lows/typhoons, and climate change.

1.1.1. Satellite Orbit

The major satellite orbits used in meteorological observation are geostationary and polar sun-synchronous. Geostationary satellites follow the earth's rotation over the equator, making them appear stationary from the earth. These include JMA's Himawari-8/9 units orbiting at 140.7°E at altitudes of approximately 35,800 km, with observation of the area from the North Pole to the South Pole at intervals of around 10 minutes for monitoring of weather disturbances and climate change. Polar-orbiting satellites observe 2,000 – 3,000 km widths across the orbit in latitudinal circulation at relatively low altitudes in short cycles (e.g., around 850 km high with 100 minutes per cycle in the NOAA series). Low-orbit observation provides higher-resolution imagery than that of geostationary satellites, but covers the same position in the sky only twice a day.

1.1.2. Observation by Himawari-8/9

Himawari-8/9 observe using a moving internal mirror that scans the earth longitudinally from the north in a stepwise fashion (Bessho et al. 2016). The figure below illustrates Himawari-8/9's complete full-disk observation (i.e., covering the entire earth as seen from the satellite) and five area observations. Himawari-8/9 observation is based on observation timeline with a basic interval of 10 minutes. The figure shows the observation areas and frequencies on a timeline of 10 minutes.

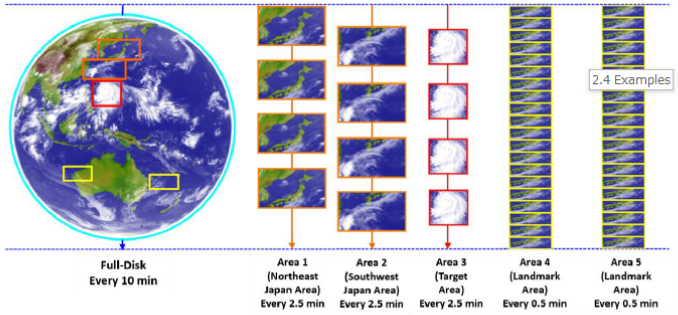

Fig. 1-1-1. Himawari-8/9 observation areas and frequencies on a timeline of 10 minutes

Himawari-8/9 perform a full-disk observation and five area observations on the timeline of 10 minutes. Two observations (i.e., 2,000-km longitudinal and 1,000-km latitudinal, as per the orange rectangles in Fig. 1-1-1) are made every 2.5 minutes over the area around Japan. These two areas are fixed, while the area in the red rectangle for typhoon monitoring (1,000-km longitudinal and latitudinal) can be changed every 2.5 minutes for specific focus on typhoons, cyclones and volcanic eruptions. In two other areas (1,000-km longitudinal, 500-km latitudinal), locations for observation can be changed every 30 seconds. This produces imagery relating to coastline characteristics as landmarks to enable correction of satellite attitude parameters based on positional differences between landmarks and predictions. The 30-second frequency of imagery capture allows monitoring of rapidly developing cumulonimbus areas that may cause extreme phenomena.

Wavelength (μm)	Himawari-8/9				Himawari-6/7		Example usages
	Band no.	Horizontal resolution (km)	Central wavelength (μm) Himawari-8	Central wavelength (μm) Himawari-9	Channel	Horizontal resolution (km)	
0.47	1	1	0.47	0.47		-	Color composite imagery, aerosols
0.51	2	1	0.51	0.51	-	-	Color composite imagery, aerosols
0.64	3	0.5	0.64	0.64	VIS	1	Color composite imagery, low cloud/fog
0.86	4	1	0.86	0.86			Vegetation, aerosols
1.6	5	2	1.61	1.61			Discrimination of cloud phases
2.3	6	2	2.26	2.26			Cloud particle radius variation
3.9	7	2	3.89	3.83	IR4	4	Low cloud/fog, natural fires
6.2	8	2	6.24	6.25	IR3	4	Upper-layer water vapor concentration
6.9	9	2	6.94	6.96			Middle-layer water vapor concentration
7,3	10	2	7.35	7.34			Middle-layer water vapor concentration
8.6	11	2	8.59	8.59			Discrimination of cloud phases, SO_2
9.6	12	2	9.64	9.63			Ozone total volume
10.4	13	2	10.41	10.41	IR1	4	Cloud imagery, cloud-top information
11.2	14	2	11.24	11.21			Cloud imagery, sea surface temperature
12.4	15	2	12.38	12.36	IR2	4	Cloud imagery, sea surface temperature
13.3	16	2	13.28	13.31			Cloud-top height

Table 1. Comparison of Himawari-8/9 and Himawari-6/7 bands. Spatial resolutions are as defined at the subsatellite point.

1.4 RGB Composite Imagery

1.4. RGB Composite Imagery

1.4.1. Principles of RGB Composite Imagery

RGB (red, green, blue) composites display satellite imagery with overlays in combinations of the three primary colors (Fig. 1-4-1).

This technique makes identification of cloud areas and obscure phenomena easier than with simpler imagery based on bands or differences. However, variables such as latitude, seasonal conditions and the characteristics of satellite-mounted radiometers may require display outside the range of standard tones, making assessment based solely on color hues more difficult in certain cases. Accordingly, it is important to fully comprehend the characteristics of the bands used in compositions.

For clarity, the global standard for RGB composite imagery has been proposed by the WMO's RGB Composite Satellite Imagery Workshop.

Fig. 1-4-1. RGB light combinations

1.4.2. RGB Composite Imagery Characteristics

This section describes WMO-standard RGB composite image from 03:00 UTC on 7 March 2016 and 18:00 UTC on 6 March 2016. The relevant phenomena may not appear with the exact precision of the colors indicated above.

(1) True Color RGB

Figure 1-4-2 shows an overlay of visible imagery from Band 3 (0.64 μm), Band 2 (0.51 μm) and Band 1 (0.47 μm) bordered in red, green and blue, respectively, producing a display similar to that seen by the human eye. It is provided on the Visible (Color) Channel in Satellite Imagery (Rapid Scan) on the JMA website. These composites have the following characteristics:

- Display of cloud and snow/ice in white for ease of discrimination from land
- Facilitated viewing of smoke, Aeolian dust (yellow sand), volcanic ash and other forms of dust (Fig. 1-4-2)
- Exclusive daytime use due to application of visible imagery

(2) Natural Color RGB

Figure 1-4-3 shows an overlay of visible image from Band 5 (1.6 μm), Band 4 (0.86 μm) and Band 3 (0.64 μm) bordered in red, green and blue, respectively, with the following characteristics:

- Band 5 (red) lower reflectance to ice crystals, resulting in regions of upper clouds and snow/ice appearing in cyan in composites of Band 4 (green) and Band 3 (blue) with higher reflectance (Fig. 1-4-4)
- High reflectance to water droplets in all three bands, causing droplet-based cloud areas (e.g., fog and low clouds) to appear in a white tone composed of the three primary colors
- Especially high Band 4 (green) reflectance against vegetation in comparison to the other two bands, causing vegetation to appear in green
- Exclusive daytime use due to application of visible and near-infrared image

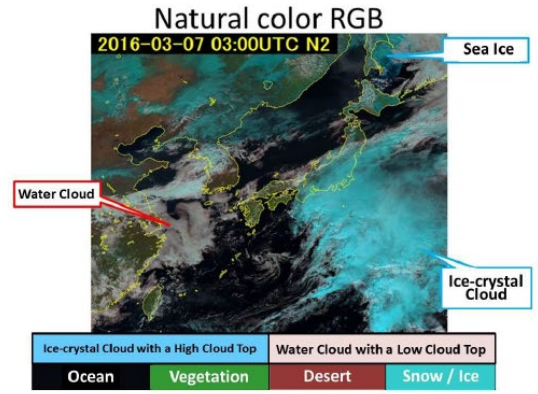

Fig. 1-4-3. Natural Color RGB sample

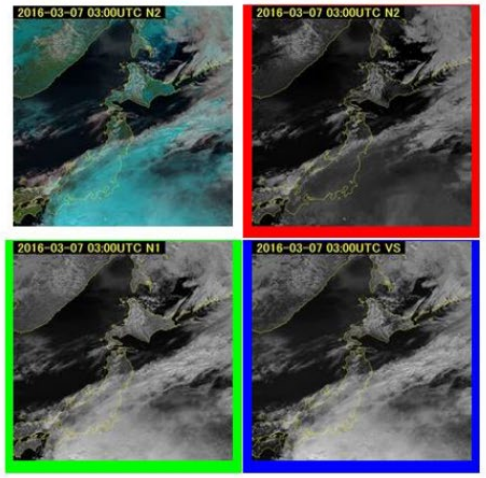

Fig. 1-4-4. Natural Color RGB composite image (top left) and source image. Top right: Band 5; bottom left: Band 4; bottom right: Band 3

Chapter 2

Cloud Type Identification via Meteorological Satellite Observation

2.4 Examples

2.4.Examples

2.4.1. Identification from Visible and Infrared Imagery

Figures 2-4-1 and 2-4-2 show examples of cloud type identification. A to G below correspond to the symbols in the figures. H and I are outlined in Section 2.4.3.

- A bright cloud area A appears between northern Hokkaido and the Sea of Okhotsk in the infrared image along the wind direction in the upper layer, with an underlying lower cloud area through it in the visible image. Hence, A is identified as thin Ci.
- The cloud area B over the sea southeast of Okinawa is Cm. This has a uniform surface and appears light grey in the infrared image because of its higher temperature as compared to A. It appears white in the visible image and stretches along the wind direction in the middle layer.
- The cloud area C at around 150 degrees east longitude to the east of Japan is St. This appears darker than surrounding cloud in the infrared image and is approximately the same temperature as the sea surface, making it difficult to identify. It appears light grey with a smooth surface in the visible image.
- The cloud area D over the East China Sea off the southwestern coast of Kyushu is Sc. It appears dark grey in the infrared image and light grey with a distinct border in the visible image.
- The partially streaky cloud area E between the Yellow Sea and the East China Sea is Cu. In the infrared image, it appears brighter than the Sc in area D. In the visible image, it appears white with clusters featuring distinct edges.
- The cloud area F (arrow marking) over the sea near the Ogasawara Islands is Cb. Its rim to the west is clear in the infrared image but obscure to the east under the influence of upper-level winds. It has a clustered appearance in the visible image with a relatively white form.
- The belt-shaped latitudinal cloud area G over the Yellow Sea is associated with a cold-air mass, as per E. However, it contains Cb and Cg, and is more developed than the Cu of E and brighter in both the infrared and visible images.

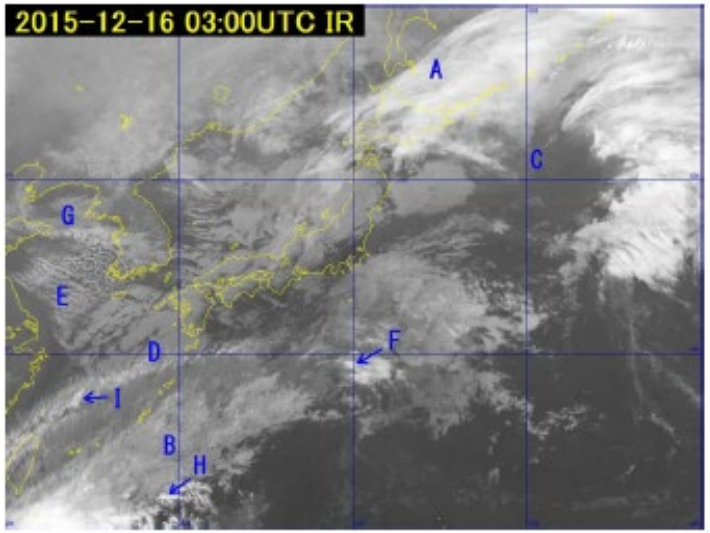

Fig. 2-4-1 B13 infrared image for 03:00 UTC on 16 December 2015

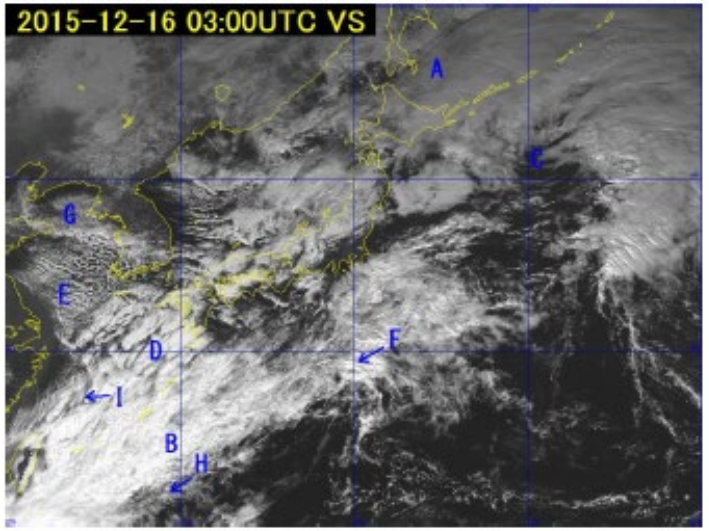

Fig. 2-4-2 B03 visible image for 03:00 UTC on 16 December 2015

2.5 Differences Between Cloud Types Identified via Meteorological Satellites and Cloud Forms in Surface Observation

2.5.2.2. Case 2: Ci Cloud Area Only

In the infrared image (Fig. 2-5-4), a straight cloud line extends from the area west of the MSC toward the prefectures of Chiba and Ibaraki. In the visible image (Fig. 2-5-5), the cloud area around the MSC appears white, but the further east it goes, the thinner and more transparent it becomes. The area around the MSC exhibits relatively thick upper-level cloud, and the area eastward shows thin upper-level cloud with an almost static western end that appears to be the origin. A photograph taken at the MSC (Fig. 2-5-6) shows the edge of the area, which can be identified as upper-level cloud both from the ground and from the satellite.

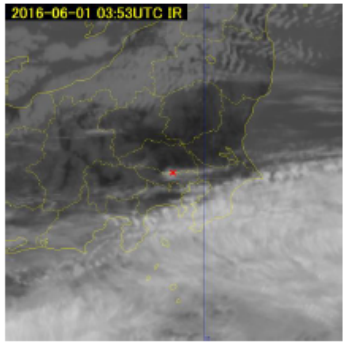

Fig. 2-5-4 B13 infrared image for 12:53 JST on 1 June 2016; red cross: MSC

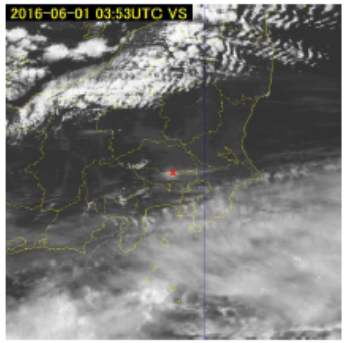

Fig. 2-5-5 B03 visible image for 12:53 JST on 1 June 2016; red cross: MSC

Fig. 2-5-6 View west from MSC for 12:53 JST on 1 June 2016. Upper-level clouds were observed from the ground.

Chapter 3
Cloud Patterns

Chapter 4

Water Vapor Patterns

Chapter 4
Water Vapor Patterns

4.1.6. Upper Troughs

Using water vapor imagery, upper troughs can be seen at the maximum cyclonic curvature of a boundary between bright and dark regions (i.e., a dark region with a convex shape to the south; Fig. 4-1-7). Troughs in the upper and middle layers can be determined from the boundary shape, and trough deepening can be estimated from the degree of darkening. From Fig. 4-1-8, a trough over Northeast China can be seen from the boundary curvature and from GSM 500 hPa contour lines.

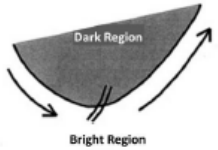

Fig. 4-1-7 Upper trough

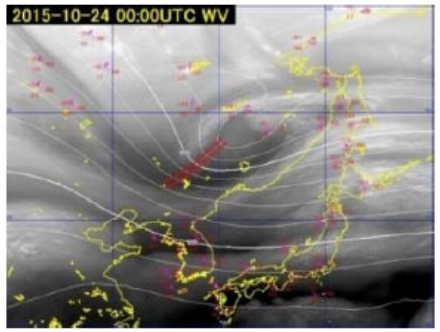

Fig. 4-1-8 Water vapor image for 00:00 UTC on 24 October 2015.
White lines: contours every 60 m (geopotential height) at 500 hPa from GSM data; red double line: upper trough.

4.3. Analysis Using Water Vapor Imagery

4.3.1. Cold Lows

Upper vortices are visualized in patterns in water vapor imagery, allowing analysis and tracking even in the absence of clouds. These often correspond to cold lows.

Figures 4-3-1 and 4-3-2 show water vapor images for an upper vortex moving eastward from the sea near the Kuril Islands. 500 hPa weather charts (Figs. 4-3-3 and 4-3-4) show that the center of the upper vortex and the cold low largely coincide.

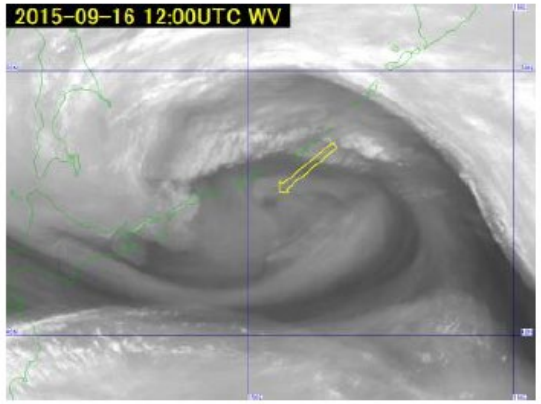

Fig. 4-3-1 Water vapor image of a cold low for 12:00 UTC on 16 September 2015

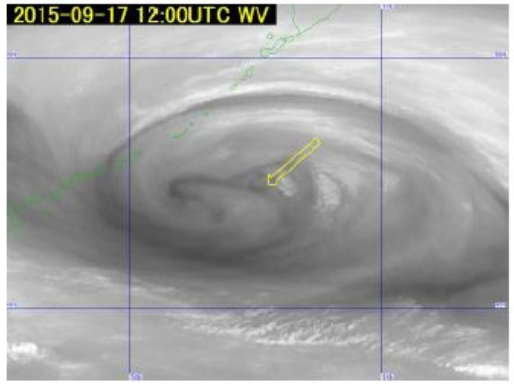

Fig. 4-3-2 Water vapor image of a cold low for 12:00 UTC on 17 September 2015

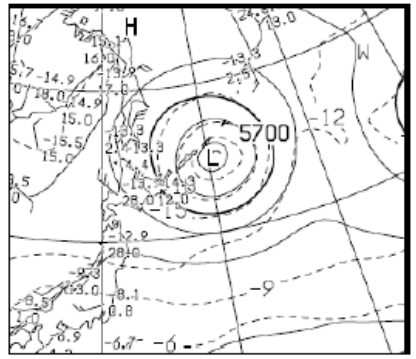

Fig. 4-3-3 500 hPa weather chart for 12:00 UTC on 16 September 2015

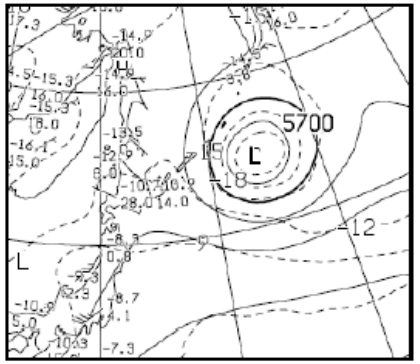

Fig. 4-3-4 500 hPa weather chart for 12:00 UTC on 17 September 2015

Chapter 5
Synoptic-scale Phenomena

Chapter 6
Meteorological Phenomena

Chapter 7
Other Phenomena

7.1 Sea Ice

7. Other Phenomena

7.1. Sea Ice

Sea ice around Japan is observed mainly in the Sea of Okhotsk and the Strait of Tartary. Its reflectance is similar to that of clouds, appearing in visible imagery as shades of grey – specifically light grey in the northern Sea of Okhotsk due to lower reflection relating to the area's high latitude and small solar elevation angles. As a result, sea ice areas may be mistaken for low clouds, but can easily be discriminated in animations due to its slower movement.

Figure 7-1-1 shows B03 visible image of sea ice east of Sakhalin Oblast and to the northeast of Hokkaido. This is easier to discriminate than in B13 infrared image from the same period (Fig. 7-1-2) due to lower temperature differences from the surrounding sea surface.

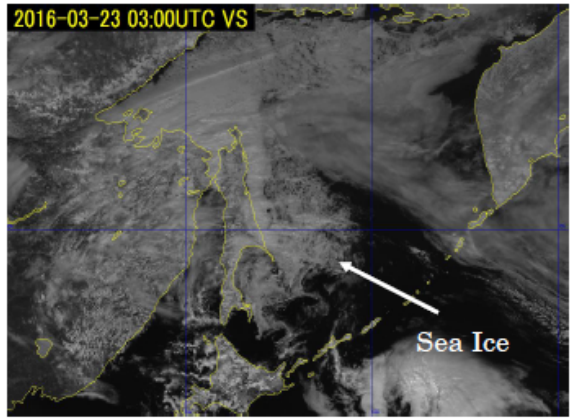

Fig. 7-1-1. B03 visible image for 03:00 UTC on 23 March 2016

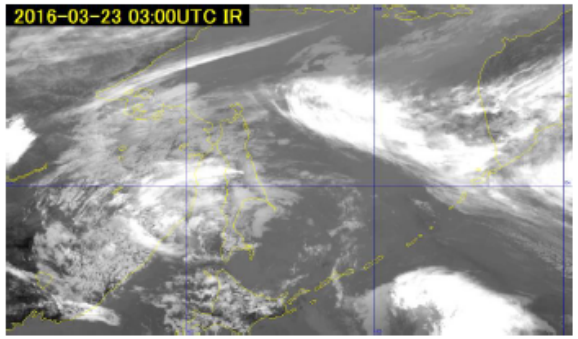

Fig. 7-1-2. B13 infrared image for 03:00 UTC on 23 March 2016

The Himawari-8 satellite Natural Color RGB composite image in Figure 7-1-3 for 05:00 UTC on 23 March 2016 shows a swirl of sea ice roughly 15 km in diameter north of the Shiretoko Peninsula, with display in cyan for easy discrimination from clouds. The vortex pattern observed is attributed to currents or wind. The swirl as a whole is too large to see from the sea or land surface, but is clear in aviation or satellite observation. Sea ice condition charts based on such imagery are issued for safety in maritime operations.

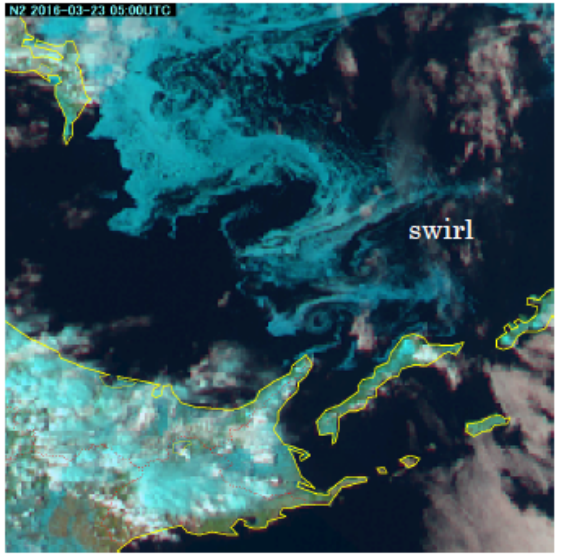

Fig. 7-1-3. Day Natural Color RGB composite image for 05:00 UTC on 23 March 2016

7.2 Snow

7.2. Snow

Snow-covered areas are displayed as white in B03 visible imagery due to high sunlight reflectance. Although identification of such areas can be challenging due to minimal temperature differences from surrounding areas, their relatively constant appearance over periods of a few days in visible imagery allows discrimination from clouds and snowfall.

Figure 7-2-1 shows B03 visible image for 19 January 2016, with mostly clear skies in the Kanto district revealing snow in white across Tokyo, Saitama, Gunma and Tochigi. Snow and clouds both appear in white, making discrimination in still imagery difficult. Discrimination is also problematic due to minimal temperature differences in the infrared imagery of Figure 7-2-2 for the same period.

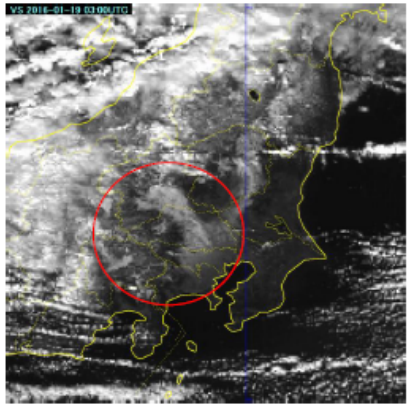

Fig. 7-2-1. Visible image for 03:00 UTC on 19 January 2016

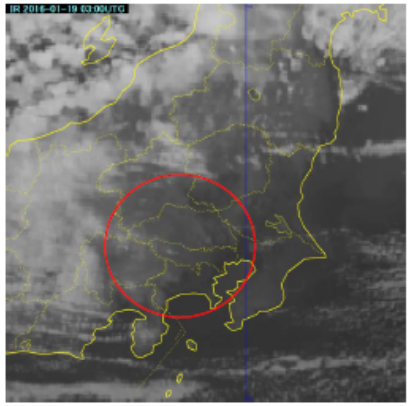

Fig. 7-2-2. Infrared image for 03:00 UTC on 19 January 2016

Figure 7-2-3 shows a Natural Color RGB composite of near-infrared and visible imagery for the same period. In the near-infrared band of B05 with an observation wavelength of 1.6 μm, the lower sunlight reflectance of ice allows discrimination from water. In Natural Color RGB composite imagery, ice crystals in upper clouds, snow areas and sea ice are all shown in cyan, enabling identification of snow areas.

Vegetation is shown in green, land surfaces in brown, and cloud/fog water particles in white.

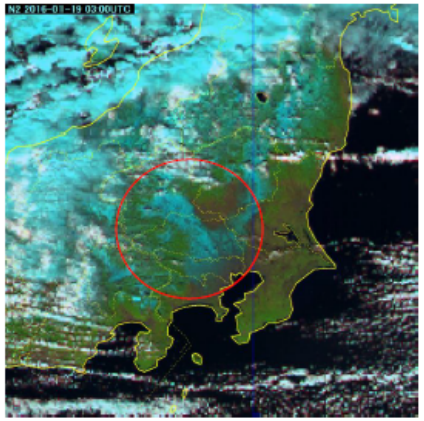

Fig. 7-2-3. Natural Color RGB composite image for 03:00 UTC on 19 January 2016

7.3 Aeolian Dust

7.3. Aeolian Dust

Figures 7-3-1 – 7-3-4 show Himawari-8 image of Aeolian dust (a.k.a. yellow dust/Kosa, which is conveyed along atmospheric currents from the Gobi Desert and the Taklamakan Desert in China) whipped up by strong cyclone-related winds around the Gobi Desert for 09:30 UTC on 9 June 2015. Figure 7-3-1 is B03 visible image showing dust spiraling up in grey, whereas True Color Reproduction RGB and Natural Color RGB composite imagery shows the dust in brown (Figs. 7-3-2 and 7-3-3, respectively). Dust RGB composite imagery specifically designed for Aeolian dust monitoring shows the phenomenon in magenta, highlighting dispersive wind-related flows.

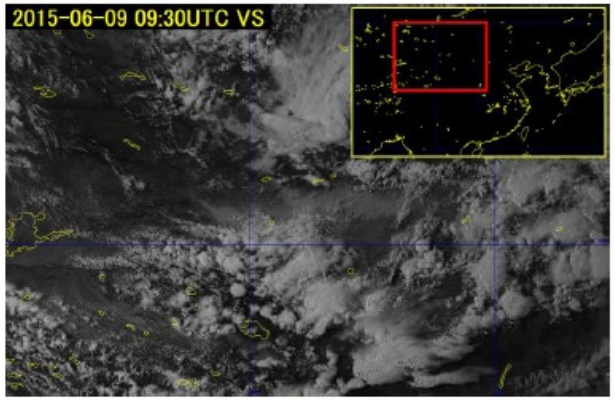

Fig. 7-3-1. B03 visible image for 09:30 UTC on 9 June 2015

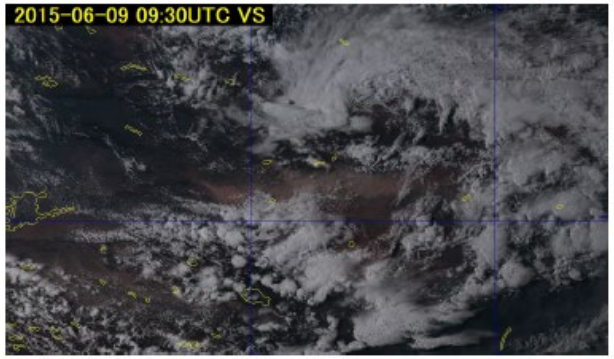

Fig. 7-3-2. True Color Reproduction RGB composite image for 09:30 UTC on 9 June 2015

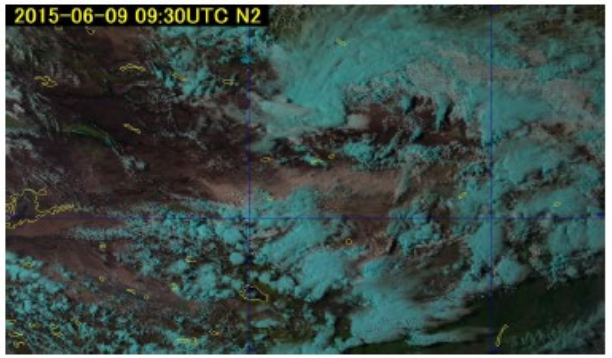

Fig. 7-3-3. Natural Color RGB composite image for 09:30 UTC on 9 June 2015

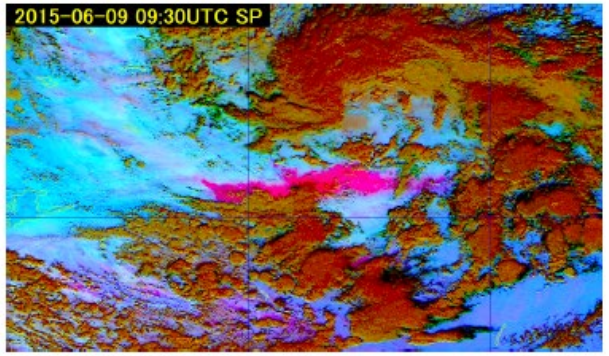

Fig. 7-3-4. Dust RGB composite image for 09:30 UTC on 9 June 2015

Figure 7-3-5 shows B03 visible image, Fig. 7-3-6 shows True Color RGB composite image, Figure 7-3-7 shows Natural Color RGB composite image, and Figure 7-3-8 shows Dust RGB composite image of Aeolian dust reaching the area around Japan for 03:00 UTC on 7 March 2016. The latter shows the dust particularly clearly in magenta.

7.4 Volcanic Eruptions

7.4.Volcanic Eruptions

Volcanic eruptions produce wind-dispersed plumes of potentially toxic ash and gas that can also adversely affect aviation safety, giving rise to a need for related prediction. In this context, data from several Himawari-8 satellite observation bands are analyzed to clarify volcanic ash and gas movement. Figure 7-4-1 shows True Color Reproduction image for a volcanic eruption on Kuchinoerabu Island at 02:10 UTC on 29 May 2015. While volcanic plumes are difficult to distinguish from surrounding clouds in monotone visible imagery, a visible imagery combination shows brownish plume content spreading westward and east-southeastward of the island.

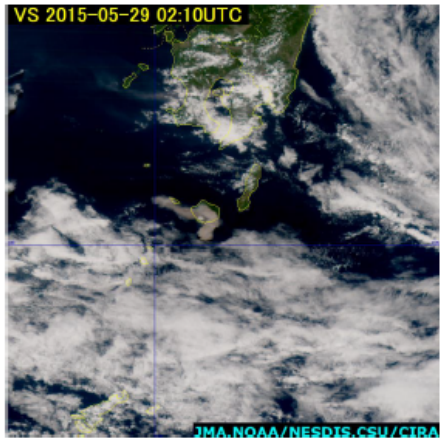

Fig. 7-4-1. B03 visible image for 09:30 UTC on 9 June 2015

Figure 7-4-2 shows Ash RGB composite image facilitating discrimination between volcanic ash and gas. It was made by combining a difference image of B13-B15 which lowers the temperature in the presence of volcanic ashes (Fig. 7-4-3) and a difference image of B13-B11 which lowers the temperature in the presence of volcanic gases (Fig. 7-4-4). The Ash RGB image shows volcanic ashes in magenta, volcanic gases in yellow-green and the overlap of the both in yellow. Following the eruption of Kuchinoerabu Island, volcanic ashes and gases were both seen.

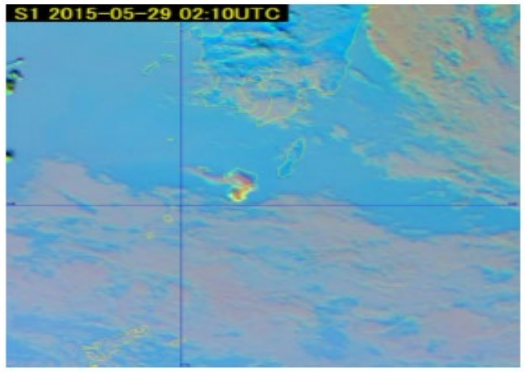

Fig. 7-4-2. Ash RGB composite image at 02:10 UTC on 29 May 2015

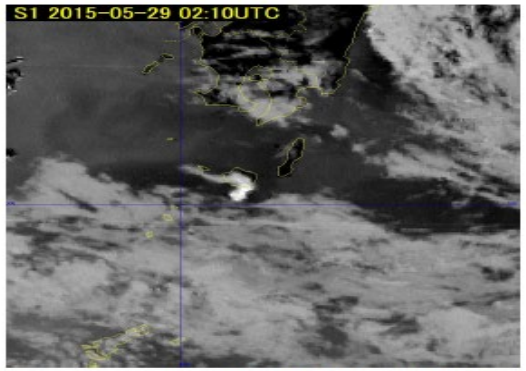

Fig. 7-4-3. Difference image of Band 15 and Band 13 at 02:10 UTC on 29 May 2015

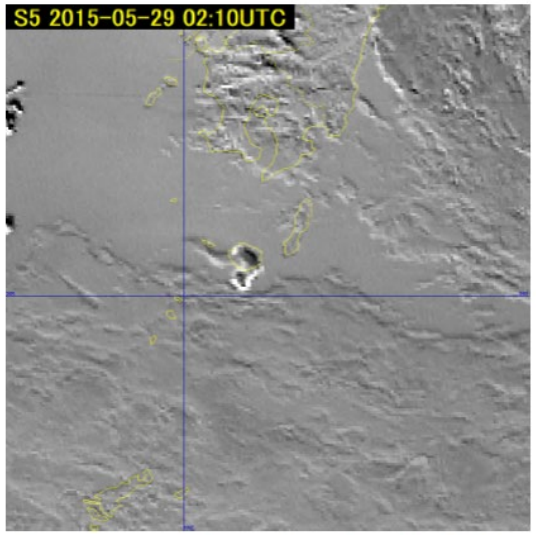

Fig. 7-4-4. Difference image of Band 13 and Band 11 at 02:10 UTC on 29 May 2015

7.5 Forest Fire and Smoke

7.5.Forest Fires and Smoke

Small-scale forest fires are difficult to identify from satellite imagery due to limited spatial resolution and observation frequency. However, the origins of larger-scale fires lasting several days can be estimated from smoke in visible imagery and hotspots in near-infrared and infrared imagery (Section 1.2: Characteristics of Each Observation Band).

Smoke from fires is often seen in visible imagery, spreading widely in a veil-like form with land and sea identifiable below, while smoke in infrared imagery cannot be seen without significant absorption. Based on these characteristics, smoke can be discriminated from clouds. The image below depicts a fire in Siberia at 07:00 on 30 April 2016. The rectangle in True Color Reproduction image contains a transparent grey area with land visible below (Fig. 7-5-1, top left), which is not seen in Band 13 image Fig. (Fig. 7-5-1, top right). Band 7 image also shows black fire hotspots (Fig. 7-5-1, bottom left), which are not observed in Band 13 image. From these observations, the grey region to the top left of Fig. 7-5-1 is assumed to be smoke capable of reaching Japan.

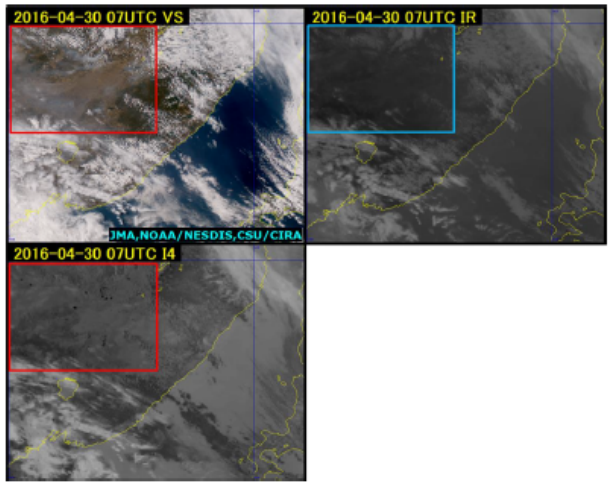

Fig. 7-5-1. Fire in Siberia at 07:00 UTC on 30 April 2016
Top left: True Color Reproduction; top right: B13 infrared; bottom left: B07 infrared

Figure 7-5-2 a from 06:00 UTC on 18 May 2016 shows a True Color Reproduction image with a white region not seen in the infrared image of Fig. 7-5-2 b. The shape/color differences from the lower clouds typically seen over the Sea of Japan suggest the presence of smoke moving from Hokkaido toward the Hokuriku and Kanto regions in correspondence with wind-direction and speed data based MSM 850-hPa analysis.

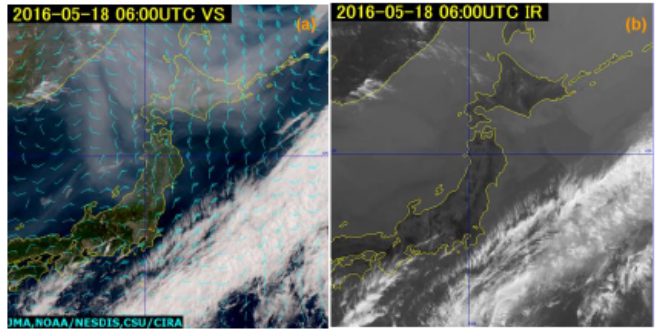

Fig. 7-5-2 Smoke from a wildfire at 06:00 UTC on 18 May 2016.
(a)True Color Reproduction image (left). (b) B13 infrared imagery (right).

Areas of burning can be determined from changes in vegetation cover. Figures 7-5-3(a)/(b) show changes relating to a fire around Lake Khanka in northeastern China. Natural Color RGB composite imagery (Fig. 7-5-3(a)) reveals a dark-brown region not seen on 14 October in northern and eastern parts of the encircled area, and many more hotspots (black dots) are seen around the lake on 25 October than on 14 October in the Band 7 imagery of Fig. 7-5-3(b). Accordingly, the region is assumed to have undergone fire damage.

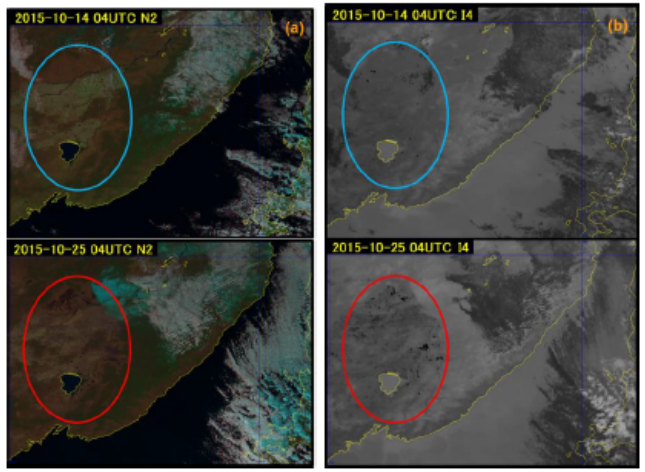

Fig. 7-5-3 Impact of wildfire around Lake Khanka.
(a) Natural Color RGB imagery (left). (b) B07 infrared imagery

Smoke from frequent major dry-season forest fires occurring in Indonesia over periods of months since the summer of 2015 is visible in satellite imagery. Figure 7-5-4(a) shows True Color Reproduction imagery revealing a thin-brown region extending from Borneo to Sumatra (not seen in the Band 13 infrared imagery of Fig. 7-5-4(b)) indicating forest fire smoke.

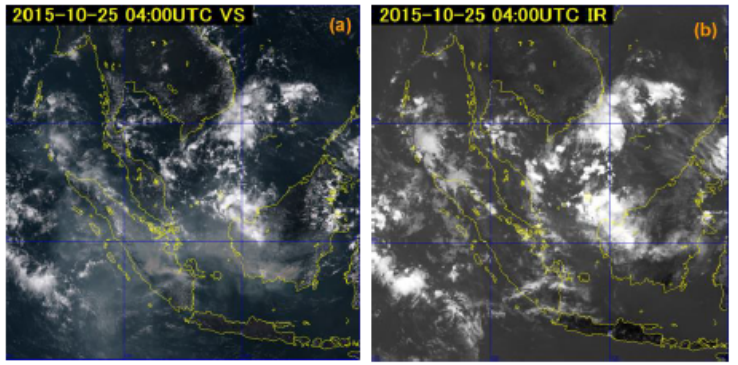

Fig. 7-5-4 Fire in Indonesia at 04:00 UTC on 25 October 2015.
(a) True Color Reproduction RGB composite image (left).
(b) B13 infrared image (right).

Thank you for your attention.

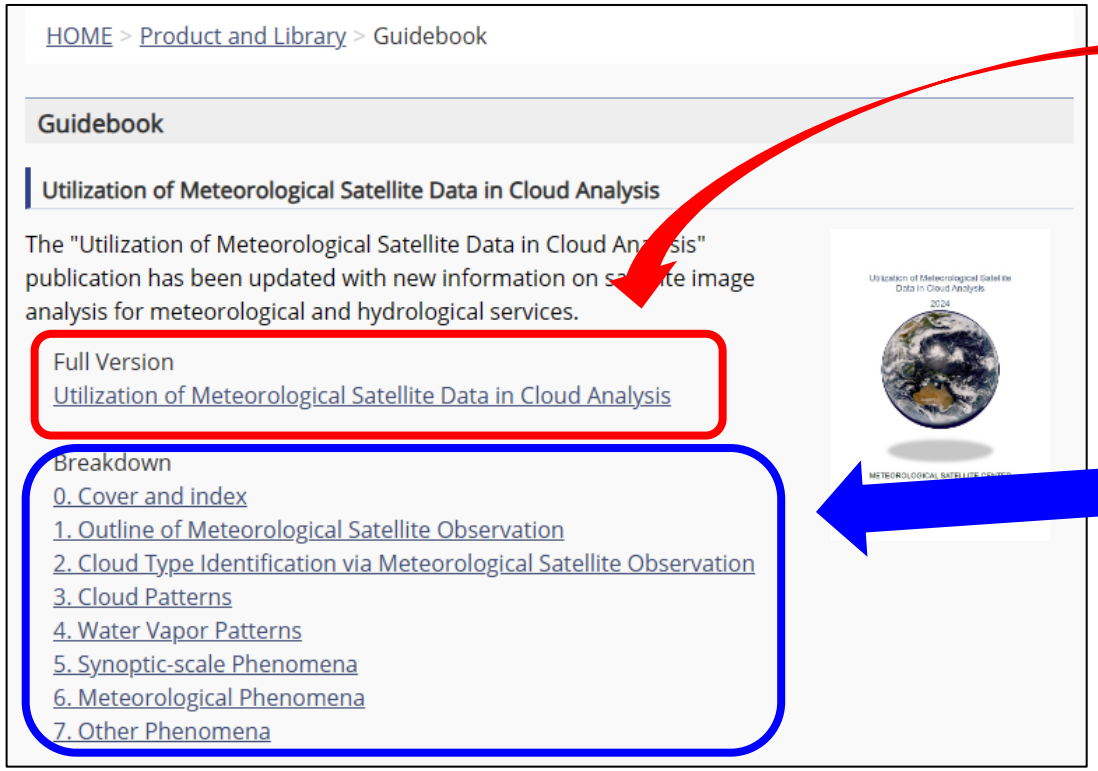

https://www.data.jma.go.jp/mscweb/en/product/library_book.html

- Download URL: https://www.data.jma.go.jp/mscweb/technotes/UtilizationMetSatData.pdf (One PDF file for all chapters)
- Breakdown PDF files for each chapter are also available.
- If you have any questions or comments about this book, please feel free to email us.
  Email: jma-msc-contact@ml.kishou.go.jp